

## **Ion motion determines multiphase performance dynamics of perovskite LEDs.**

*Jevgenij Chmeliov, Karim Elkhoully<sup>#</sup>, Rokas Gegevičius, Lukas Jonušis, Andrius Devižis, Andrius Gelžinis, Marius Franckevičius, Iakov Goldberg, Johan Hofkens, Paul Heremans, Weiming Qiu,\* Vidmantas Gulbinas\**

Dr. J. Chmeliov, R. Gegevičius, L. Jonušis, Dr. A. Devižis, Dr. A. Gelžinis, Dr. Marius Franckevičius, Prof. V. Gulbinas

Department of Molecular Compound Physics

Center for Physical Sciences and Technology

Saulėtekio Avenue 3, Vilnius LT-10257, Lithuania

E-mail: vidmantas.gulbinas@ftmc.lt

Dr. J. Chmeliov, Dr. A. Gelžinis, Prof. V. Gulbinas

Institute of Chemical Physics

Faculty of Physics

Vilnius University

Saulėtekio Avenue 9, Vilnius LT-10222, Lithuania

K. Elkhoully, I. Goldberg, Prof. P. Heremans, Dr. W. Qiu

Imec, Kapeldreef 75, 3001 Leuven, Belgium

K. Elkhoully, I. Goldberg, Prof. P. Heremans,

Department of Electrical Engineering

KU Leuven, Kasteelpark Arenberg, 3001 Leuven, Belgium

Prof. Johan Hofkens, Dr. W. Qiu

Department of Chemistry, KU Leuven, Celestijnenlaan 200F, 3001 Leuven, Belgium.

<sup>#</sup> K. Elkhoully contributed equally to the work as the first author.

\* Corresponding author

**Keywords:** Perovskite, LED, ion migration, electroluminescence, dynamic operation

## Abstract

Perovskite LEDs (PeLEDs) are currently reaching up to about 20% external quantum efficiency and becoming a promising technology for display and lighting applications. Still, many questions regarding their performance remain unclear, particularly those related to stability, operation in non-stationary regimes, and efficiency roll-off at high current densities. Here, we address some of those issues in LEDs based on MAPbI<sub>3</sub> perovskite. We analyse electroluminescence (EL) and current dynamics during and after application of sequences of voltage pulses, at different temperatures. Analysis of the results suggests that the complex dynamics observed on time scales from sub-seconds to minutes and hours can be explained by the redistribution of mobile species characterised by about 175 meV activation energy, most likely iodine interstitials. This redistribution alters the carrier injection, spatial electric field and carrier density distributions and density of nonradiative recombination centres. Mathematical modelling of the ion motion and related processes enabled us to mimic the EL and current dynamics and to disentangle complex sequence of processes determining the PeLED operation.

## 1. Introduction

Perovskite light-emitting diodes (PeLEDs) are a promising technology for development of wavelength tuneable, large-area, solution-processed, flexible light sources.<sup>[1-6]</sup> These devices have already demonstrated external quantum efficiencies (EQE) exceeding 20%.<sup>[4-6]</sup> However, many problems still remain unsolved, limiting the widespread usage of PeLEDs. One of them, inherent to all perovskite devices, is the short-term and long-term stability. PeLEDs also suffer from efficiency roll-off limiting their brightness.<sup>[7-10]</sup> A further issue, particularly important for the high-

speed device operation, is the occurrence of hysteresis<sup>[1,11]</sup> and variations of the electroluminescence EQE and photoluminescence (PL) efficiency<sup>[3,12]</sup> under electrical stress.

The performance hysteresis in perovskite solar cells was widely investigated and was attributed to the modifications of perovskite-transport layer interfaces or to the motion of mobile ions.<sup>[13–16]</sup> Ion motion in metal halide perovskites is a very complex and still poorly understood phenomenon. Generally, all constituents of metal halide perovskites - halides, lead, and organic cations - may form vacancies, interstitials and anti-sites, which may be mobile and act as carrier traps.<sup>[16–18]</sup> On the other hand, theoretical evaluations show that only few of them form deep traps acting as non-radiative recombination centres,<sup>[17]</sup> while shallow traps have a negligible effect on a trap-assisted recombination.<sup>[19]</sup>

Recently, several papers reported the persistent enhancement of the EQE of PeLED, observed during initial minutes or even hours of its operation under applied positive voltage (so-called stressing regime), and attributed it to the motion of the mobile excess iodine ions that fill vacancies and reduce concentration of iodine interstitials, acting as deep carrier traps.<sup>[3,20]</sup> Similar gradual performance enhancement under positive bias voltage was also reported for perovskite solar cells and was likewise attributed to the motion and recombination of ions and vacancies.<sup>[21]</sup> On the other hand, Wang et al. observed reversible changes of the EQE of PeLED and also ascribed them to the motion of iodine ions.<sup>[2]</sup> Recently, Cheng et al. reported that diffusion of organic cations from the perovskite to the electron-transporting layer was responsible for the EQE roll-off.<sup>[22]</sup> Leijtens. et al. attributed reversible changes, observed on a time scale of several minutes, to the motion of methylammonium cations (MA<sup>+</sup>).<sup>[23,24]</sup> Meanwhile Liu et al. observed lateral drift of MA<sup>+</sup> ions during tens of seconds on a surprisingly large, more than tens of micrometers distances.<sup>[25]</sup>

Consequently, there is a general consensus that ion motion is the key factor responsible for the dynamic changes of the efficiency of perovskite-based devices. However, the reported time scales, intensities of the observed changes, and their attribution to some particular kinds of ions are very different. Overall, the underlying physical mechanisms of the ion motion-induced variations in device performance still remain far from clear.

Herein, we report a detailed study of the ion motion that causes both persistent and reversible changes of the PeLED performance, taking place on time scales ranging from

milliseconds to hours. Temperature dependencies revealed identical activation energies for all these processes occurring on different time scales. We suggest a mechanism explaining the majority of the observed changes by motion of a single type of charged defects and their recombination with “counter” defects acting as recombination centres. The validity of our model is supported by numerical simulations.

## 2. Experimental results and discussion

### 2.1 EL and current dynamics

We first investigated the EL and current dynamics of a PeLED based on MAPbI<sub>3</sub> perovskite under abrupt application of the pump voltage. The device structure, and the corresponding energy level diagram are presented in Figure 1. Description of the PeLED fabrication procedures can be found in the experimental section, while Figure S1 in SI gives IV characteristics and voltage dependence of electroluminescence EQE of the device stabilised after 30 min. operation.

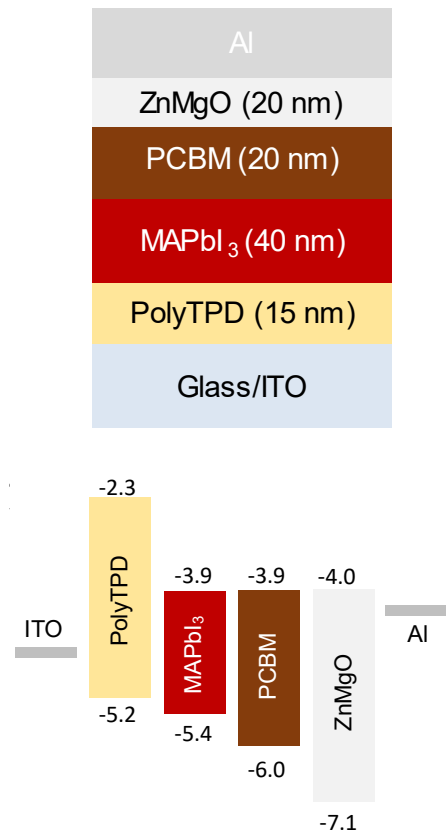


**Figure 1. The PeLED structure and corresponding energy level diagram.**

We have shown in our previous work that the use of PCBM/ZnMgO electron injection layer significantly improves the device stability<sup>[26]</sup>, which ensures the reliable and reproducible measurements in this study. After abrupt first-time application of a constant voltage to the PeLED, over just several minutes, we observe a significant growth of the electroluminescence (EL) intensity and electric current. Figure 2a presents normalized EL intensity and current growth kinetics at different device temperatures after application of 2 V voltage. Since the first-time voltage application can be studied only once, curves at different temperatures were measured for different devices formed on the same substrate.

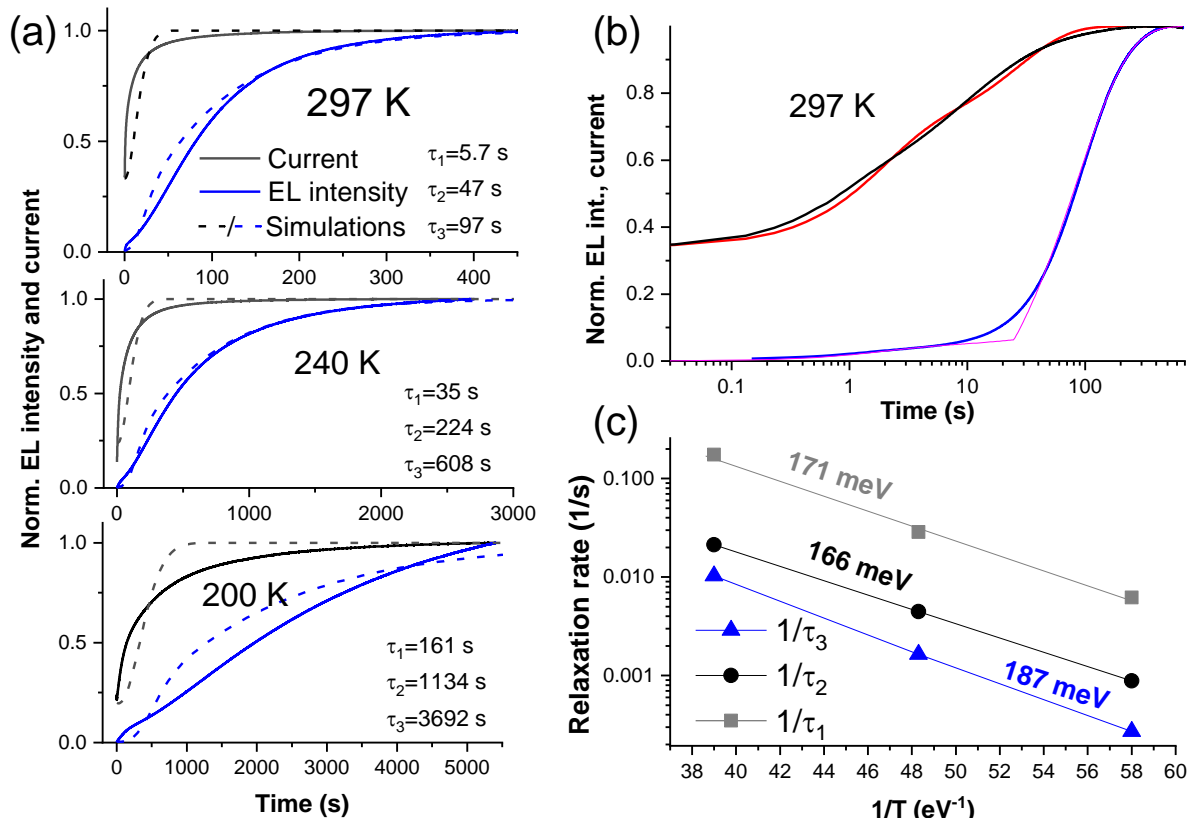


**Figure 2. EL and current dynamics at different temperatures in pristine PeLEDs under first-time application of 2 V voltage.** a) Normalised EL (blue lines) and current (black lines) growth kinetics, measured (solid lines) and simulated (dashed lines, see below for discussion) at three different

temperatures (kinetics at different temperatures were measured for different samples, formed on the same substrate). b) Current and EL kinetics at room temperature on a logarithmic time scale (black and blue lines, respectively), red and magenta lines show approximations by eqs. 1 and 2 respectively. c) Arrhenius plot for the slow EL growth time constant  $\tau_3$  (blue), fast current growth time constant  $\tau_1$  (grey line), and slow current growth time constant  $\tau_2$  (black).

Immediately after the voltage was applied, the EL intensity was very weak, but it increased and reached a plateau after several minutes at room temperature and after more than one hour at 200 K. Similar behaviour of perovskite LEDs has been reported before<sup>[3]</sup> and was denoted as stressing. The electrical current was non-vanishing from the very beginning and then increased 3–5 times, but the growth rate was significantly faster than that of EL. Figure 2b shows the current and EL kinetics at 297 K on a logarithmic time scale, more clearly demonstrating the initial growth dynamics. The initial current was almost constant during tens of milliseconds and created almost no EL during this time. It should be noted that the delayed growth of the EL cannot be explained by the charging of the sample capacitance since this process, according to the device RC characteristics, should take place on a timescale of several microseconds, i.e. about  $10^4$  times faster. Therefore, the initial absence of EL suggests that either a) the initial current is created by injection of only one kind of charge carriers, which then leak to the opposite electrode creating no EL, or b) EL is absent because of fast nonradiative recombination. The EL starts to grow after about 100 ms, and up to about 10 s, it grows simultaneously with current. Nevertheless, the EL intensity during the initial  $\sim 10$  s remains low. Faster growth starts only when current almost stabilises, which suggests that the later growth process is not related to the carrier injection.

The current growth kinetics can be reasonably well (see red line in Figure 2b) fitted with the bi-exponential rise functions as:

$$I(t) = I_0 + a_1[1 - \exp(-t/\tau_1)] + a_2[1 - \exp(-t/\tau_2)], \quad (1)$$

resulting in time constants of  $\tau_1 = 1.7$  and  $\tau_2 = 25$  s at room temperature (RT). We have also successfully fitted the EL kinetics (magenta line in Figure 2b) using the same time constants  $\tau_1, \tau_2$  and correspondingly modified coefficients  $a_1$  and  $a_2$  and additional delayed slow saturating growth component:

$$EL(t) = a'_1[1 - \exp(-t/\tau_1)] + a'_2[1 - \exp(-t/\tau_2)] + b[1 - \exp(-(t - \Delta t)/\tau_3)], \quad (2)$$

here we consider that the third component equals to zero before  $t > \Delta t$ . The best fit gives  $\Delta t = 25$  s and  $\tau_3 = 97$  s. These fitting results show that the weak EL intensity during initial several tens of seconds is proportional to the growing current part, while the strongly increasing EL phase starts after delay of about 25 s. Similar fitting has been also performed for the lower temperature data. The obtained time constants are listed in Figure 2a.

Following earlier publications discussed in the Introduction, it is natural to attribute the observed processes to the motion of ions. We presented the time constants, obtained from the EL and current rise kinetics at different temperatures (Figure 2a), in Arrhenius coordinates (see Figure 2c), which enable us to evaluate activation energies  $E_a^i$  of ions, responsible for different processes:

$$k_i = k_{i0} \exp\left(-\frac{E_a^i}{k_B T}\right), \quad (3)$$

here  $k_i = \tau_i^{-1}$ ,  $k_B$  is Boltzmann constant and  $T$  is the absolute temperature. The Arrhenius plot gives surprisingly identical, within the experimental accuracy, activation energies of about 175 meV for all three processes, strongly suggesting that all of them have the same physical origin, i.e. they are related to the same type of ion motion.

There is a large diversity in literature regarding the mobile ions. According to the theoretical investigations, iodine interstitials and vacancies have the lowest motion activation energies, in different publications ranging from about 80 meV to more than 800 meV.<sup>[16,18,27,28]</sup> Very similar activation energy values ( $E_a = 137 \pm 28$  meV and  $190 \pm 50$  meV) as obtained by us have been evaluated experimentally from PL enhancement by the light soaking data and attributed to the motion and annihilation of iodine interstitials and vacancies.<sup>[29,30]</sup> Similar motion activation energies have been also reported for another halide  $\text{Br}^-$  ions.<sup>[31–33]</sup> On the other hand, reported activation energies for migration of  $\text{MA}^+$  and  $\text{Pb}^+$  ions typically exceed 500 meV. These attributions are in line with other publications claiming that iodine defects are particularly important in optoelectronic devices since they can easily move under application of electric field.<sup>[27,29,34,35]</sup> According to Dong et al., motion of negatively charged iodine interstitials  $\text{I}^-$  takes place on a timescale of tens of seconds.<sup>[31]</sup> Similar conclusion that redistribution of iodine defects causes reversible variations of current and EL intensity on a time scale of seconds has been also

recently suggested by analysing performance hysteresis of FAPbI<sub>3</sub> PeLEDs.<sup>[11]</sup> According to Buin et.al., positively charged iodine vacancies V<sub>i</sub><sup>+</sup> should be the most mobile charged iodine defects.<sup>[17]</sup> However, our samples were prepared under iodine-rich conditions from solution with 20 mol% excess PMAI (benzylammonium iodide), which suggests that iodine interstitials inside the bulk of crystallites or iodine ions at the crystallite boundaries should be dominating defects.<sup>[17,18]</sup> Although we cannot completely exclude role of other kinds of charged mobile species, iodine interstitials I<sub>i</sub> seem to be the most likely mobile species mainly responsible for the observed PeLED performance dynamics.

To get more information about the stressing properties, we have modified our investigation technique to decouple monitoring of the LED parameters from the stressing impact. For stressing, we applied 100 mA/cm<sup>2</sup> current density (voltage was about 1.7 V) for different time intervals and after each stressing interval we monitored the LED status by using a series of rectangular pulses of 1.45 V in amplitude and 5 μs in duration, applied with 30 μs period for 30 ms (see Figure S2 in SI for time sequence of electrical pulses). These short low-voltage monitoring pulses only weakly affected the LED performance. Such investigation protocol enabled us to separate the PeLED stressing and monitoring of its parameters. It also enabled us to investigate the recovery of the PeLED performance after the stressing current was terminated, as well as the effect of other impacts such as negative voltage and light soaking. To get more information about the PeLED status, we have also simultaneously monitored current and the EL spectrum. In a similar way we could also monitor stressing-induced changes of the perovskite electroabsorption, sample capacitance, photoluminescence (PL) intensity and its decay kinetics.

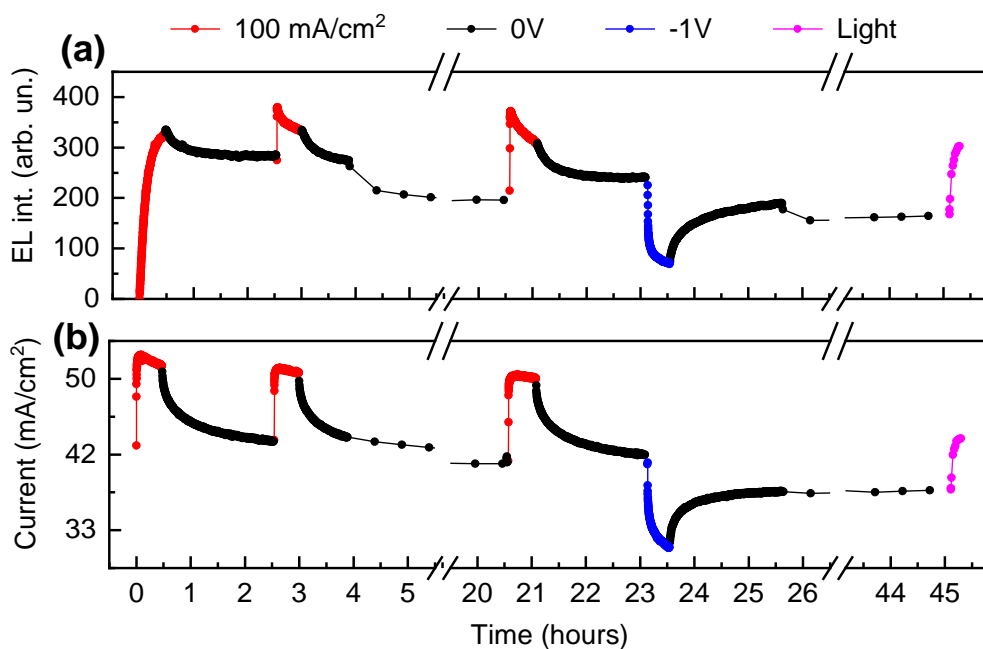


**Figure 3. Stressing-induced processes monitored by pump pulse trains.** EL intensity (a) and current (b) dynamics monitored by short positive voltage pulses of 1.45V, during following types of stress and relaxation: stressing by 100 mA/cm<sup>2</sup> current (red points); relaxation at zero applied voltage (black points); stressing by negative -1V voltage (blue points); light soaking at 0V voltage (magenta points).

Figure 3 shows the EL and current kinetics, measured for the fresh sample affected at different time intervals by positive (red points), or negative (blue points) voltage, during relaxation at zero applied voltage (black points), as well as under light soaking by 1sun intensity light at 0 V (magenta points). Similar to the case of continuous stressing (Figure 2a), the initial EL intensity of the non-stressed sample was very weak. The EL growth was 2–3 times slower than observed with 2 V steady state voltage, which was apparently caused by the weaker current created by lower used stressing voltage of 1.7 V. The current growth was less significant than under application of constant voltage, apparently because of non-negligible impact of monitoring pulses.

After termination of the stressing voltage, both EL and current gradually decreased. The current decreased to the same value as it was before stressing, while the EL intensity decreased only by

less than 20%. Moreover, the decay rates of both EL and current kinetics were very similar. Second application of the stressing voltage after 2.5 hours and the third application after 22 hours caused very fast EL growth even to a higher value than the value reached during the first stressing session. Surprisingly, after this fast initial rise, the EL intensity slowly decreased during the second and third stressing sessions, unlike the steady increase during the first session.

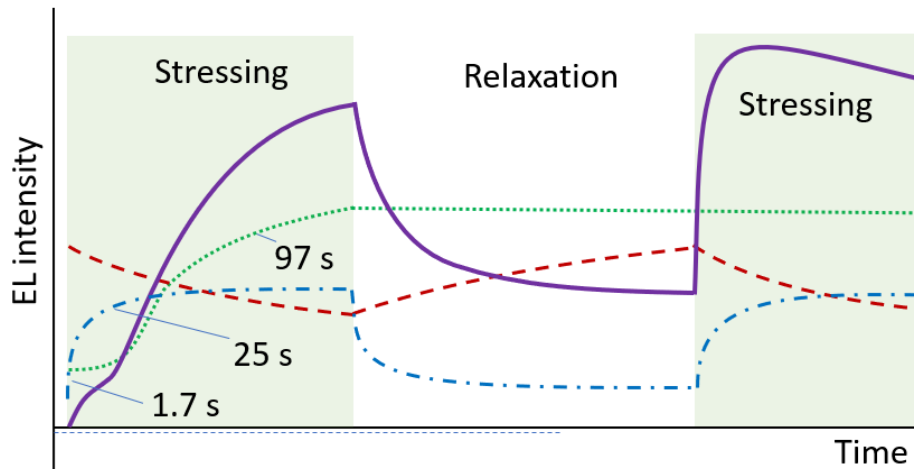


**Figure 4. Major stressing-induced processes.** EL development kinetics (solid magenta line), bi-exponential current growth causing fast reversible EL growth component (dash-dot blue line), slow irreversible EL growth component (dot green line), and reversible EL decay (dash red line). The numbers show time constants of various processes at room temperature at 2 V stress voltage obtained from exponential fitting.

The above-described experimental data lead to the stressing scenario schematically presented in Figure 4. We suggest that the EL intensity is determined by three processes: fast reversible EL growth congruous with the bi-componental saturating current growth with time constants  $\tau_1$  and  $\tau_2$ ; slow persistent EL growth with time constant  $\tau_3$ ; and reversible EL decay. The time constants vary depending on the applied voltage and temperature. This model naturally explains the two striking differences observed during the first and subsequent stressing sessions, i.e. larger EL intensity and its decay observed during subsequent stressing sections.

To get more insight into the stressing dynamics and independently verify this proposed multi-component scheme, we have additionally measured stressing-induced dynamics of several other PeLED parameters: EL wavelength, photoluminescence efficiency and its decay kinetics, sample capacitance, and electroabsorption. Stressing-induced changes of these parameters are presented in Figure 5. Below we discuss these data sequentially by analysing the stressing-induced processes presented in Figure 4.

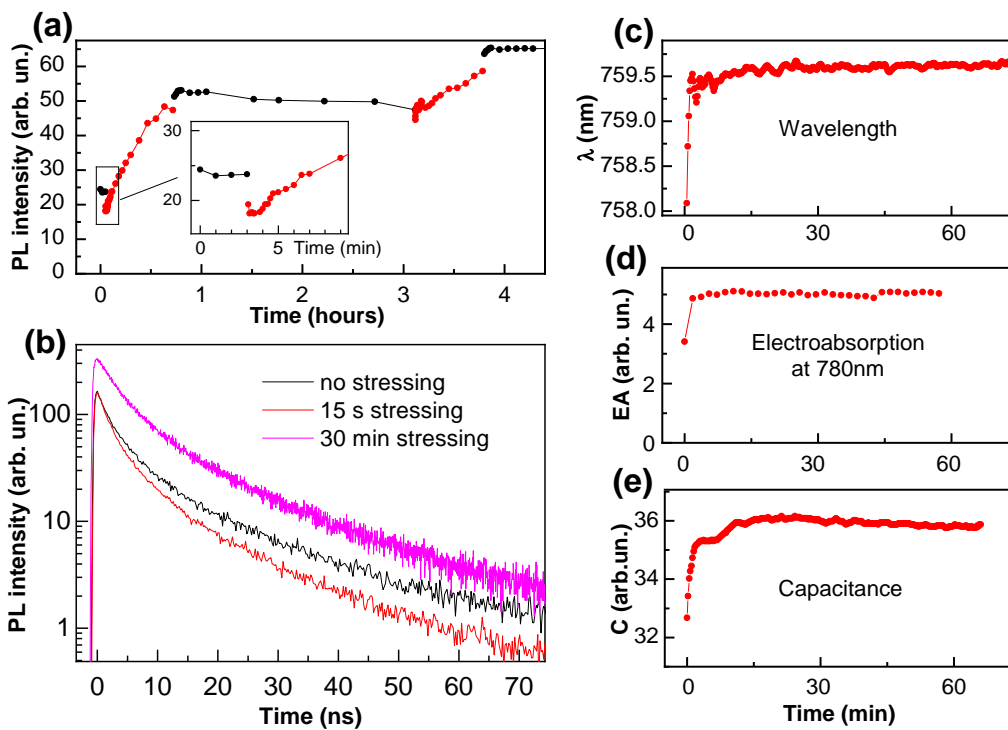


**Figure 5. Changes of various PeLED parameters, induced by stressing with 100 mA/cm<sup>2</sup> current.** a) PL intensity dependence on stressing time (red points) and relaxation at applied zero voltage (black points), b) PL decay kinetics in sample stressed for different time intervals, c) wavelength of the EL band maximum, d) electroabsorption at 780 nm and e) capacitance kinetics during sample stressing.

## 2.2 Stressing-induced processes

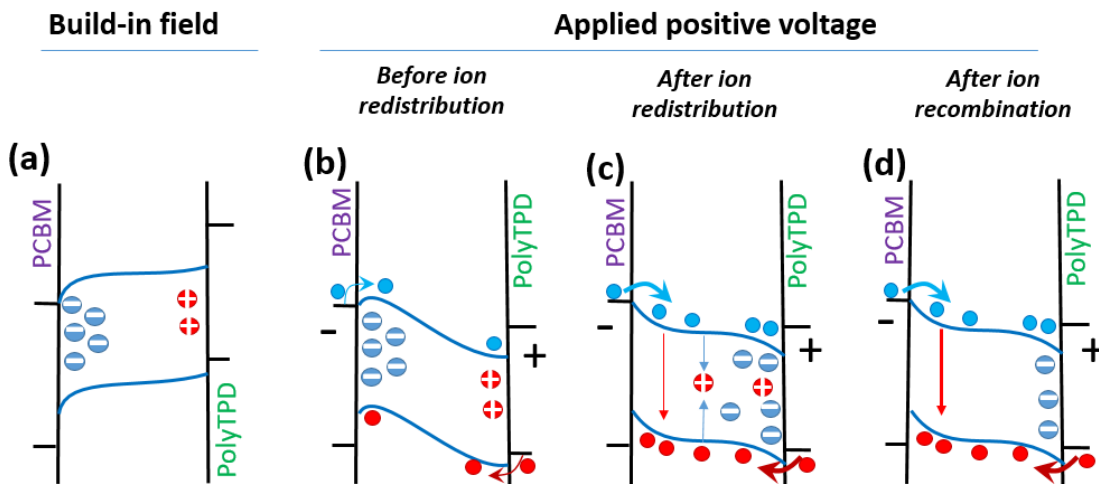
**Fast reversible current and EL growth.** As shown in Figure 2b, this initial evolution phase expressed as growth of current together with emergence and initial development of EL continues for about 20 s at RT. We will consider how other PeLED parameters change during this time. Figure 5a shows the photoluminescence intensity dynamics monitored during the sample stressing. The PL intensity was measured at zero applied voltage, when stressing voltage was temporary switched off. As shown in the inset in Figure 5a, the PL intensity slightly drops down during initial tens of seconds, i.e., during the initial evolution phase. Afterwards it increases more than 2.5 times during the slow irreversible EL growth phase discussed below. Termination of the stress voltage causes a fast PL intensity increase again.

Figure 5b shows the PL decay kinetics, which reveals a bi-exponential decay. The kinetics were measured at zero applied voltage after stressing the sample for the indicated time intervals. Comparing PL decay kinetics before and after 15 s of initial stressing, we observe that the fast stressing-induced PL intensity drop is mainly caused by faster PL decay on a time scale of tens of ns. We have also measured the PL decays for non-stressed sample under applied different negative and positive voltages not reaching EL operation threshold. These kinetics are presented in SI Figure S3. The applied voltage mainly changes the slow decay phase, apparently by varying electric field inside the perovskite layer and, thus carrier extraction. It implies that the faster PL decay observed for the shortly stressed sample may also be caused by the modification of the electric field within the perovskite film. This assumption is supported by the electroabsorption (EA) measurements (see Figure 5d), which show an increase of the EA signal after a short-time stressing. The EA signal is proportional to the square of the electric field strength, therefore changes of the EA signal shall be considered as an indication of the redistribution of the electric field strength over perovskite layer thickness. Additional support is also provided by the capacitance measurements that demonstrate capacitance increase during the fast stressing phase (see Figure 5e), indicating that the electric field in the stressed sample concentrates in thinner perovskite layer. The initial fast stressing phase also changes the EL spectrum; the luminescence peak wavelength exhibits a slight red shift (Figure 5c). The shift in emission wavelength was attributed to the interference of EL radiation emitted towards transparent electrode and that reflected from the metal electrode; the red shift indicates that the recombination zone moves away

from the interface with the electron transporting layer.<sup>[26,36]</sup> Thus, this is another indication that the fast stressing phase changes the electric field distribution and consequently also the distribution of charge carriers inside the perovskite layer.

All the above discussed observations are consistent with conclusion that the fast phase is caused by the ion motion, which changes the electric field distribution within the perovskite layer. Although this conclusion is quite expected, the experimental data described above also give important information enabling us to consider the shape of the electric potential and its modifications during stressing, which leads to the changes of carrier injection and recombination. We suggest the qualitative model schematically presented in Figure 6. At zero applied voltage, different work functions of electrodes create build-in electric field inside the perovskite layer of opposite direction than electric field in operating PeLED. This field accumulates negative mobile I<sup>-</sup> ions next to the PCBM electron transport layer, while positive ions accumulate next to the hole transporting layer. The accumulated ions partly or completely screen the electric field in the central part of the perovskite layer. The field screening would be non-symmetrical, as shown in Figure 6a in case of different concentrations of positive and negative ions. This potential shape suggests that the flat potential in the central perovskite layer part causes slow extraction of photogenerated charge carriers, therefore pristine sample exhibits relatively weak PL quenching (as shown in Figure 5b) caused by the carrier extraction.

Application of the stressing voltage does not change the ion distribution instantaneously, therefore the initial shape of the potential becomes as shown in Figure 6b. This potential shape creates additional barriers for the carrier injection, while additional barrier for the hole injection of about 200 meV is created by the difference between work functions of perovskite and hole transporting material PolyTPD (see Figure 1). The barriers for electrons and holes are different, therefore injection of one kind of charge carriers may be almost completely blocked causing very low electroluminescence.



**Figure 6. Schematic representation of potential surfaces and ion distributions at different phases of the PeLED stressing.** a) under built-in electric field, I<sup>-</sup> ions (blue symbols) and vacancies V<sup>+</sup> (red symbols) accumulate next to PCBM and PolyTPD electrodes respectively, b) abrupt application of stressing voltage creates electric field potential with barriers for electron and hole injection, and creates only weak EL because of the spatial separation of electron and hole densities, c) redistribution of I<sup>-</sup> ions and vacancies (assumed being less mobile) reduces barriers for both electrons and holes and also causes ion recombination, d) EL intensity increases when ion recombination eliminates majority of vacancies acting as recombination centres.

Subsequently, applied stressing voltage causes drift of ions away from the transporting layers, thus reducing the barriers for the carrier injection. Finally, ions change their positions causing reduction of injection barriers. The potential shape becomes as shown in Figure 6c, enabling efficient injection of both electrons and holes and, thus, more efficient EL. However, the roles of positive and negative ions seem to be significantly different in our samples. This is because: a) identical activation energies obtained for different processes strongly suggest that one kind of mobile ions strongly dominate and b) concentration of iodine interstitials in our iodine-rich samples is expected to be much larger than that of iodine vacancies. Figure 6 accounts for the dominating role of I<sup>-</sup> ions.

**Slow permanent EL growth.** As shown in Figure 2b, this slow (tens of minutes) stressing phase starts with a delay of about 25 s at RT after application of the stressing voltage and causes major enhancement of the EL intensity, while current remains at the same level as reached during the previous fast stressing phase. The slow stressing phase also causes almost 3-fold permanent

enhancement of the PL intensity (Figure 5a). As shown in Figure 5b, the slow stressing phase increases the initial intensity of the PL kinetics, slackens its decay during initial 10 ns, but does not change the PL decay on a  $t > 10$  ns time scale (compare red and magenta curves obtained after 15 s and 30 min stressing). We attributed the PL kinetics at  $t > 10$  ns to the carrier extraction, thus this process does not change during the slow stressing phase. While the fast initial PL decay should be attributed to the carrier trapping. Therefore, EL and PL growth during the slow stressing phase is a manifestation of the enhanced radiative recombination efficiency, apparently caused by the reduced non-radiative Shockley-Read-Hall (SRH) recombination related to the carrier trapping. This conclusion is supported by the increased open circuit voltage of the stressed PeLED operating as solar cell (see Figure S4 in SI for IV curves under artificial solar illumination), which is also an indication of the reduced nonradiative relaxation. This slow phase, as was discussed, is characterised by the same activation energy as the fast phases, strongly suggesting that it is also related to the motion of iodine ions.

Similar PL enhancement of MAPbI<sub>3</sub> perovskites, only induced by optical soaking, is a well-known phenomenon. It was explained by excitation-induced spatial redistribution and recombination of iodine interstitials and vacancies,<sup>[29,30]</sup> which act as recombination centres. Such recombination is not possible in PeLEDs before their stressing because, according to our model, the built-in electric field concentrates iodine ions and vacancies in narrow layers next to the opposite transport layers, they are spatially separated and cannot recombine. Applied stressing voltage drags ion populations towards each other, they mix together as shown in Figure 6c and start to recombine. Thus, the delayed start of the slow permanent EL growth phase at about 25 s corresponds to the time needed for charged species to redistribute across the perovskite layer and mix together. Recombination of the iodine defects lasts for about 10 min at RT and longer at lower temperatures. The recombination rate of iodine defects is proportional to the diffusivity of more mobile species, therefore the rate of this process as well as processes attributed to the ion redistribution is characterised by the same activation energy. Recombination of the iodine interstitials and vacancies permanently reduces concentration of recombination centres. In case of different ion and vacancy concentrations, the minor species, in our case V<sup>+</sup>, suffer relatively larger losses.

***Reversible EL decay.*** This reversible process observed as partial decay of the EL intensity during the repeatable device stressing (Figure 3) and presented by the red line in diagram in Figure 4

reduces the EL intensity, but does not change significantly the current, photoluminescence, EL wavelength and electroabsorption (Figures 3 and 5). This process reveals a fast component of several minutes and a much slower decay on a time scale of hours. During the first-time stressing this decay process is masked by EL increase discussed above. During the repeatable stressing, the fast decrease phase apparently also competes with the EL growth causing slightly faster EL saturation in comparison with the current. Similar decay processes have been observed and investigated in detail in previous publications.<sup>[20,26]</sup> The fast decay component has been attributed to the sample heating due to current flow, while the slow component is apparently related to the partly reversible device degradation, probably also related to ions.

**Relaxation after stressing.** Termination of the stress voltage causes simultaneous decay of the current and EL intensity (Figure 3 black points), because recreated built-in electric field drags ions back to their initial positions as in pristine sample recreating barriers for the carrier injection. However, the initial state of pristine sample does not recover completely because of irreversible reduction of the trap and ion densities, as discussed below. It should be also noted that the current and EL decays during relaxation are much slower than their growth during repeatable stressing, although both processes are expected to be caused by the motion of Ions. According to the above presented ion redistribution model, the stressing and relaxation processes shall not be identical. First, because of different electric field strengths and its spatial distributions. Recombination of  $I^-$  with  $V^+$ , reduces the ion density and may also change the dynamics. The stressing and relaxation processes may also be different because ion motion during the PeLED stressing takes place in the presence of charge carriers, while charge carriers are absent during relaxation. Ion diffusivity has been reported being enhanced by optical excitation, however the mechanism of this phenomenon still remains vague.<sup>[37]</sup> Thus, ion diffusivity may be enhanced by charge carriers, both photogenerated and injected, which makes ion motion faster during stressing.

### 2.3 Impact of reverse bias and light soaking

**Impact of negative voltage.** Application of the negative voltage to the stressed sample after its relaxation at zero voltage caused additional decay of the EL intensity and current (see Figure 3, blue points). Reinforcement of the internal electric field above the built-in value caused stronger accumulation of ionic species and additionally increased barriers for the carrier injection. After

termination of the negative voltage, current and EL intensity gradually recover to the values characteristic of stressed samples at zero applied voltage (see Figure 3).

Application of the negative voltage for a long time interval revealed an additional slow EL decay and almost completely quenched the EL after 25 hours (see Figure S5 in SI). We speculate that strong negative voltage applied for the long time may cause redistribution of less mobile ions, probably  $\text{MA}^+$ , which additionally increase barriers for the carrier injection. Subsequent application of a positive stressing voltage returned the device to the strongly electroluminescent state again.

**Light soaking.** We have also attempted to investigate the influence of light soaking on the PL and EL intensities by illuminating the PeLED by 1 sun intensity light, similar as was used in ref. [29,30]. Surprisingly, no significant changes of the PL intensity and its decay kinetics have been observed in pristine non-stressed samples (see Figure S6c in SI). The light soaking, however, increased the current of non-stressed sample by about 20% and approximately doubled the EL intensity (see Figures S6a and b in SI), which, however, remained about 10 times lower than after current-stressing. Consequently, the influence of the light soaking was similar to the one produced by the fast-stressing phase. The light soaking of the stressed sample also caused similar changes as additional current stressing, i.e. increased the current and EL intensity, which relaxed later when the light soaking was terminated.

Our above presented model explains this unusual influence of light soaking in a similar way as was proposed for perovskite solar cells, where redistribution of ions or vacancies was suggested to be driven by photoinduced voltage creating additional electric field.<sup>[38]</sup> Optical excitation of PeLED generates an open circuit voltage like in solar cells. Consequently, it reduces the build-in electric field similarly as an applied positive voltage. The reduced internal electric field causes redistribution of iodine ions, that leads to the reduction or complete disappearance of barriers for the carrier injection, and, as a consequence, increase in current and EL.

### **3. Numerical modelling of the stressing-induced processes.**

To further verify the suggested stressing mechanism, we have modelled the ion redistribution processes and related PeLED performance dynamics. The model is described in SI. Briefly, we

calculated ion distribution at zero applied voltage, when the electric field inside perovskite is determined by the built-in voltage. Next, we calculated the electric field potential immediately after a positive PeLED pumping voltage was applied. Assuming that carrier transport layers are in exhaustible carrier sources, considering that mobility of charge carriers is several orders of magnitude larger than that of mobile ions, and accounting for the charge carrier recombination and their drift in the electric field produced by the external applied voltage and internal distribution of ions and carriers themselves, we calculated the resulting stationary distribution of electrons and holes in perovskite layer as well as their current density. Assuming that small variations in ion density do not significantly change the distribution of the net electric field in the perovskite, we then propagated ion dynamics for a small-time interval, recalculated stationary distributions of charge carriers and iteratively repeated the cycle. As a result, we obtained not only the gradual ion redistribution in the net electric field created by applied voltage, ions, and charge carriers, but also the effect of this redistribution onto the electric current and spatial densities of the electrons and holes. During these calculations, we accounted for carrier recombination without distinguishing between radiative and nonradiative parts assuming just a constant bimolecular recombination rate. For the sake of simplicity we consider motion of only negative iodine ions, which, as was discussed, likely are dominating players.

As already mentioned, our model directly gives time dependence of the current density on a time scale of seconds, and, finally, we calculate the EL intensity as follows. We assume that the EL intensity is proportional to the spatial overlap of the electron,  $n(x)$ , and hole,  $p(x)$ , densities multiplied by efficiency of radiative recombination,  $\xi(t)$ , which changes due to the current stressing:

$$EL(t) \propto \xi(t) \cdot \int n(x, t)p(x, t)dx. \quad (4)$$

Here, the integral is taken across the perovskite layer. For simplicity, we also assume that the current stressing rate is proportional to the current density, thus the efficiency of the radiative recombination equals to:

$$\xi(t) = 1 - \exp(-k_{\text{str}}j(t) t), \quad (5)$$

here  $j(t)$  is current density and  $k_{\text{str}}$  is the stressing rate constant.

The model contains a number of variable parameters. Some of them such as carrier mobilities, bimolecular recombination rate, ion density, were chosen based on literature data, others evaluated from the sample structure and geometry, remaining are free parameters varied to achieve a reasonable agreement with the experimental data. The parameter values used in our calculations are listed in Table S1 in SI.

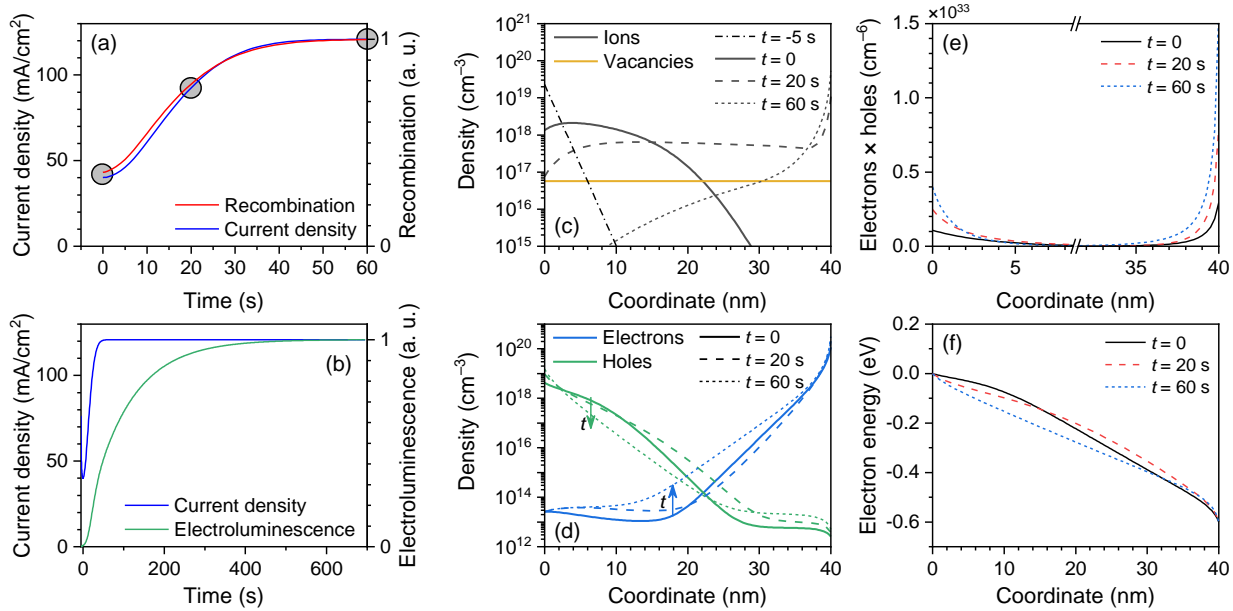


**Figure 7. Simulated perovskite stressing dynamics.** a) Time dependence of the current density ( $j(t)$ , blue line, left axis), and spatial overlap of the electron and hole densities ( $\int n(x, t)p(x, t)dx$ , red line, right axis) during the initial fast stressing phase. b) Dynamics of the current density and EL intensity during the slow stressing phase. c) Ion densities within the perovskite layer (0 nm and 40 nm coordinates correspond to the interfaces with PCBM and Poly TPD respectively), calculated at three delay times, shown with shaded circles in panel a (black lines). Density of immobile ion vacancies remained constant (yellow line). d) Calculated densities of electrons (blue lines) and holes (green lines) at the same three delay times. e) Distributions of the spatial overlap of carrier densities,  $n(x, t) \cdot p(x, t)$ , calculated at the same three delay times. f) Calculated electrostatic energy of the electron in the perovskite layer at the same three delay times, the insert shows electric field strength next to Poly TPD layer. In panels c--f, point  $x = 0$  corresponds to the interface with the electron transporting layer.

Figure 7a shows current and recombination rate dynamics during the initial fast stressing phase, evaluated for optimal parameter values, while Figure 7b shows also an EL dynamics on a longer time scale. The latter was calculated according to Eq. 5. For comparison with experimental data, the evaluated current and EL dynamics at different temperatures are also presented with dashed lines in Figure 2a. A reasonable agreement with experimental data has been obtained except of the very initial times. Processes at lower temperatures were calculated just assuming that the ion mobility decreases with temperature as described by eq. 3 with activation energy  $E_a=181$  meV, which is close to the activation energies determined from Figure 2c.

Our inability to reproduce the very initial dynamics indicates that some additional fast processes take place, which were not included into the model. In our calculations, we consider that the ion mobility is constant. While in case of the disordered material, the initial ion motion may be significantly faster than determined by their mobility at longer times, as was observed for carrier motion in disordered organic semiconductors.<sup>[39]</sup> Such dispersive ion motion would cause much faster initial current growth, and its slower saturation at longer times, as observed experimentally. The fast initial electric field redistribution may also be caused by the presence of the slow component of the dielectric permittivity, which could be present in perovskites due to ferroelectric polarization.<sup>[40]</sup> We cannot also completely exclude that our attribution of the observed processes to the motion of iodine interstitials is incorrect. Some evaluations suggest dynamics during tens and hundreds of seconds may be caused by motion of MA or Pb defects, while motion of iodine defects should be much faster.<sup>[16]</sup> Thus, motion of iodine defects may be responsible for the dynamics during subseconds and several initial seconds. However, so far we don't have arguments in favour of one or another process.

Figures 7c and d show spatial distributions of mobile negative and immobile positive ions as well as electrons and holes, calculated at three time moments: 1) immediately after application of positive voltage, 2) in the intermediate stage of ion redistribution phase, and 3) after the complete ion redistribution. Figures 7e and f also show distributions of electron energy and of product of electron and hole densities determining carrier recombination rate and, thus, electroluminescence intensity. The initial ion distribution is determined by the built-in electric field corresponding to about 1.2 V built-in voltage created by the differences between work functions of transport layers and electrodes. Correspondingly, applied positive voltage of 2 V in the ideal case creates potential

difference on the perovskite layer equal to 0.8 V. However, apparently a fraction of the applied voltage drops on transport layers, therefore we consider potential difference across perovskite layer being of 0.6 V under applied 2 V voltage. Immediately after voltage application, the initial ion distribution creates a potential energy surface for electrons exhibiting a flat zone close to the negative electrode, which limits the electron injection. On the other hand, the hole injection is limited by the barrier of about 200 meV originating from the difference between HOMO levels of PolyTPD and MAPbI<sub>3</sub>. This barrier narrows when electrons and negative iodine ions accumulate next to the PolyTPD layer and create strong electric field as shown in insert in Figure 7F, enabling faster hole injection by tunnelling, hence increase of the hole density at the positive electrode (point  $x = 40$  nm). Consequently, when iodine ions redistribute and gradually accumulate next to PolyTPD layer, both electron and hole injection rates increase which in turn lead to the increase in carrier density and recombination rate.

As shown in Figure 7e, the carrier recombination takes place close to the perovskite layer surfaces where charge carriers accumulate. Before the ion redistribution, stronger carrier recombination takes place close to the negative Al electrode. Later on, due to ion diffusion, recombination intensifies along the positive ITO electrode, which is in agreement with the observed red shift of the EL wavelength (see Figure 5c) that, indicating shift of the recombination zone away from the metal electrode.<sup>[26,36]</sup> Concentration of the electric field in a thin layer (insert in Figure 7f) shall lead to increase in the electroabsorption signal and in sample capacitance, in agreement with the experimental data (see Figures 5d and e).

Even though the used calculations simplify some of the processes taking place in real PeLEDs, they quite closely reproduce the current and EL dynamics and also qualitatively explain changes of the PL wavelength, electroabsorption and capacitance taking place during the PeLED stressing. Depending on the PeLED structure and properties of the perovskites used, processes in other PeLEDs may be significantly different. Figure S6 shows how the current and EL dynamics change under variation of some model parameters. Quantitative similarity retains by changing carrier mobility, ion density by orders of magnitude, but significantly changes depending on the applied potential difference across perovskite layer. Consequently, our investigations suggest major principles enabling to understand and predict the PeLED operation dynamics, which is an important step in their further development.

## **Conclusions.**

EL intensity and current of MAPI PeLED show complex growth kinetics after application of constant pump voltage. The initial EL intensity of pristine sample is very weak and grows hundreds of times on time scales of milliseconds to tens of minutes. Subsequent application of voltage after the device “rests” for tens of minutes or hours creates much stronger initial EL, which additionally grows by tens of percent during seconds. We analysed the EL growth processes by using several investigation techniques that enabled us to investigate changes of EL intensity, current, and EL spectrum taking place during current stressing, relaxation after stressing, application of negative voltage or light soaking. Additionally, we investigated stressing induced changes of the sample photoluminescence, electroabsorption and capacitance.

Analysis of the experimental results together with mathematical modelling revealed that the complex changes taking place on several very different time scales are caused by motion of ions characterised by activation energies of about 175 meV. Our experimental results and literature data suggest that negative iodine ions play a dominating role. Redistribution of the spatial distribution of ions along the perovskite layer thickness changes shape of electric potential, barriers for carrier injection and also causes of their recombination with iodine interstitials acting as nonradiative recombination centres.

We believe that the obtained deeper understanding of the processes taking place in operating PeLEDs will be important for their optimization directed to more efficient performance particularly in dynamic regimes.

## **Experimental section**

**Device fabrication.** Fabrication of the LEDs was described elsewhere.<sup>[20]</sup> Briefly, PolyTPD was spin coated on the precleaned ITO substrates at 4000 rpm for 40 s and then anneal at 150 °C for 20 min, followed by treating with O<sub>2</sub> plasma for 6 s at a power of 100 W to improve surface wettability. Afterwards, MAPbI<sub>3</sub> with 20 mol% extra benzylammonium iodide was deposited on PolyTPD in a N<sub>2</sub> filled glove box, using an antisolvent method. Then, PCBM solution in

chlorobenzene was deposited at 3000 rpm, followed by depositing ZnMgO nanoparticles in ethanol at 4000 rpm. The devices were finished by thermal evaporation of 100 nm Al. The device area is defined by the shadow mask and was  $0.125 \text{ cm}^2$  with dimensions of  $2.5 \text{ mm} \times 5 \text{ mm}$ .

**Investigation techniques.** EL and current dynamics under application of steady state voltage were measured using Keithley 2604B dual channel SMUs. The sample was mounted in vacuum in a JANIS vpf-100 liquid nitrogen cryostat, where the sample temperature was controlled using a Lakeshore 335 temperature controller. A Silicon photodiode 818-SL from Newport was used to monitor the EL signal. The sampling rate was set to 100 ms for both channels. The experiment starts by applying a DC voltage to the PeLED, while the current and EL dynamics are simultaneously monitored using the two SMUs.

Pulsed stressing measurements were performed according to protocol presented in SI. Briefly the sample was stressed by  $100 \text{ mA/cm}^2$  current for variable time durations and subsequently EL intensity, current and mean EL wavelength were measured by switching-off the stressing voltage and applying train of short electrical probing pulses. The voltage was applied by using arbitrary function generator Tektronix AFG3101 and current was measured with Agilent Technologies DS05054A oscilloscope using  $50 \ \Omega$  input. EL intensity and spectrum were measured with AvaSpec-HS1024x58/122 fiber optic spectrometer (Avantes). The same procedure was used to investigate the light soaking impact, only in this case 1 sun light intensity was applied instead of stressing current. During investigations of the relaxation processes, the sample, between probing pulses, was kept at zero voltage in dark.

Photoluminescence, electroabsorption and capacitance were investigated by using the same stressing protocol, but measurements were performed at zero applied voltage. Capacitance measurements were performed by using the same setup by applying sinusoidal voltage and measuring alternative current passing through the device. The relative capacitance changes were evaluated from the current amplitude and phase shift.

Electroabsorption measurements were performed as described in ref.<sup>[41]</sup> The electroabsorption signal was measured by comparing absorption spectra at positive and negative 1V voltages. The positive 1V voltage compensated the built-in voltage, thus the net potential difference across the perovskite layer was close to zero. While at -1 V applied voltage the potential difference was of about 2 V.

Time-resolved PL measurements were performed by the Edinburgh Instruments Time Correlated Single Photon Counting (TCSPC) spectrometer. Picosecond pulsed diode laser EPL-470 emitting 72 ps pulses at 470 nm with the repetition rate of 500 kHz (interval 2  $\mu$ s) was used for the sample excitation.

## References

- [1] Z.-K. Tan, R. S. Moghaddam, M. L. Lai, P. Docampo, R. Higler, F. Deschler, M. Price, A. Sadhanala, L. M. Pazos, D. Credgington, F. Hanusch, T. Bein, H. J. Snaith, R. H. Friend, *Nature Nanotech* **2014**, *9*, 687.
- [2] J. Wang, N. Wang, Y. Jin, J. Si, Z.-K. Tan, H. Du, L. Cheng, X. Dai, S. Bai, H. He, Z. Ye, M. L. Lai, R. H. Friend, W. Huang, *Adv. Mater.* **2015**, *27*, 2311.
- [3] L. Zhao, J. Gao, Y. L. Lin, Y.-W. Yeh, K. M. Lee, N. Yao, Y.-L. Loo, B. P. Rand, *Adv. Mater.* **2017**, *29*, 1605317.
- [4] Y. Cao, N. Wang, H. Tian, J. Guo, Y. Wei, H. Chen, Y. Miao, W. Zou, K. Pan, Y. He, H. Cao, Y. Ke, M. Xu, Y. Wang, M. Yang, K. Du, Z. Fu, D. Kong, D. Dai, Y. Jin, G. Li, H. Li, Q. Peng, J. Wang, W. Huang, *Nature* **2018**, *562*, 249.
- [5] W. Xu, Q. Hu, S. Bai, C. Bao, Y. Miao, Z. Yuan, T. Borzda, A. J. Barker, E. Tyukalova, Z. Hu, M. Kawecki, H. Wang, Z. Yan, X. Liu, X. Shi, K. Uvdal, M. Fahlman, W. Zhang, M. Duchamp, J.-M. Liu, A. Petrozza, J. Wang, L.-M. Liu, W. Huang, F. Gao, *Nat. Photonics* **2019**, *13*, 418.
- [6] T. Chiba, Y. Hayashi, H. Ebe, K. Hoshi, J. Sato, S. Sato, Y.-J. Pu, S. Ohisa, J. Kido, *Nature Photon* **2018**, *12*, 681.
- [7] C. Murawski, K. Leo, M. C. Gather, *Adv. Mater.* **2013**, *25*, 6801.
- [8] M. Yang, N. Wang, S. Zhang, W. Zou, Y. He, Y. Wei, M. Xu, J. Wang, W. Huang, *J. Phys. Chem. Lett.* **2018**, *9*, 2038.
- [9] W. Zou, R. Li, S. Zhang, Y. Liu, N. Wang, Y. Cao, Y. Miao, M. Xu, Q. Guo, D. Di, L. Zhang, C. Yi, F. Gao, R. H. Friend, J. Wang, W. Huang, *Nat Commun* **2018**, *9*, 608.
- [10] A. Fakhruddin, W. Qiu, G. Croes, A. Devižis, R. Gegevičius, A. Vakhnin, C. Rolin, J. Genoe, R. Gehlhaar, A. Kadashchuk, V. Gulbinas, P. Heremans, *Adv. Funct. Mater.* **2019**, *29*, 1904101.
- [11] H. Wang, Z. Chen, J. Hu, H. Yu, C. Kuang, J. Qin, X. Liu, Y. Lu, M. Fahlman, L. Hou, X. Liu, F. Gao, *Adv. Funct. Mater.* **2021**, *31*, 2007596.
- [12] R. Gegevičius, M. Franckevičius, J. Chmeliov, W. Tress, V. Gulbinas, *J. Phys. Chem. Lett.* **2019**, *10*, 1779.
- [13] H. J. Snaith, A. Abate, J. M. Ball, G. E. Eperon, T. Leijtens, N. K. Noel, S. D. Stranks, J. T.-W. Wang, K. Wojciechowski, W. Zhang, *J. Phys. Chem. Lett.* **2014**, *5*, 1511.
- [14] H.-W. Chen, N. Sakai, M. Ikegami, T. Miyasaka, *J. Phys. Chem. Lett.* **2015**, *6*, 164.
- [15] W. Tress, N. Marinova, T. Moehl, S. M. Zakeeruddin, M. K. Nazeeruddin, M. Grätzel, *Energy Environ. Sci.* **2015**, *8*, 995.
- [16] J. M. Azpiroz, E. Mosconi, J. Bisquert, F. De Angelis, *Energy Environ. Sci.* **2015**, *8*, 2118.
- [17] A. Buin, P. Pietsch, J. Xu, O. Voznyy, A. H. Ip, R. Comin, E. H. Sargent, *Nano Lett.* **2014**, *14*, 6281.
- [18] W.-J. Yin, T. Shi, Y. Yan, *Appl. Phys. Lett.* **2014**, *104*, 063903.
- [19] E. Aydin, M. Bastiani, S. Wolf, *Adv. Mater.* **2019**, *31*, 1900428.
- [20] K. Elkhoully, R. Gehlhaar, J. Genoe, P. Heremans, W. Qiu, *Adv. Optical Mater.* **2020**, *8*, 2000941.
- [21] J. Wu, Y. Li, S. Tan, B. Yu, H. Li, Y. Li, J. Shi, H. Wu, Y. Luo, D. Li, Q. Meng, *ACS Appl. Mater. Interfaces* **2020**, *12*, 27258.
- [22] T. Cheng, G. Tumen-Ulzii, D. Klotz, S. Watanabe, T. Matsushima, C. Adachi, *ACS Appl. Mater. Interfaces* **2020**, *12*, 33004.
- [23] T. Leijtens, E. T. Hoke, G. Grancini, D. J. Slotcavage, G. E. Eperon, J. M. Ball, M. De Bastiani, A. R. Bowring, N. Martino, K. Wojciechowski, M. D. McGehee, H. J. Snaith, A. Petrozza, *Adv. Energy Mater.* **2015**, *5*, 1500962.
- [24] Y. Yuan, J. Chae, Y. Shao, Q. Wang, Z. Xiao, A. Centrone, J. Huang, *Adv. Energy Mater.* **2015**, *5*, 1500615.
- [25] Y. Liu, A. V. Ievlev, N. Borodinov, M. Lorenz, K. Xiao, M. Ahmadi, B. Hu, S. V. Kalinin, O. S. Ovchinnikova, *Adv. Funct. Mater.* **2021**, *31*, 2008777.
- [26] K. Elkhoully, I. Goldberg, H. Boyen, A. Franquet, V. Spampinato, T. Ke, R. Gehlhaar, J. Genoe, J. Hofkens, P. Heremans, W. Qiu, *Adv. Optical Mater.* **2021**, 2100586.
- [27] C. Eames, J. M. Frost, P. R. F. Barnes, B. C. O'Regan, A. Walsh, M. S. Islam, *Nat Commun* **2015**, *6*, 7497.
- [28] J. Haruyama, K. Sodeyama, L. Han, Y. Tateyama, *J. Am. Chem. Soc.* **2015**, *137*, 10048.
- [29] E. Mosconi, D. Meggiolaro, H. J. Snaith, S. D. Stranks, F. De Angelis, *Energy Environ. Sci.* **2016**, *9*, 3180.
- [30] D. W. deQuilettes, W. Zhang, V. M. Burlakov, D. J. Graham, T. Leijtens, A. Osherov, V. Bulović, H. J. Snaith, D. S. Ginger, S. D. Stranks, *Nat Commun* **2016**, *7*, 11683.
- [31] Q. Dong, J. Mendes, L. Lei, D. Seyitliyev, L. Zhu, S. He, K. Gundogdu, F. So, *ACS Appl. Mater. Interfaces* **2020**, *12*, 48845.

- [32] S. Meloni, T. Moehl, W. Tress, M. Franckevičius, M. Saliba, Y. H. Lee, P. Gao, M. K. Nazeeruddin, S. M. Zakeeruddin, U. Rothlisberger, M. Graetzel, *Nat Commun* **2016**, *7*, 10334.
- [33] A. Oranskaia, J. Yin, O. M. Bakr, J.-L. Brédas, O. F. Mohammed, *J. Phys. Chem. Lett.* **2018**, *9*, 5474.
- [34] C. Li, A. Guerrero, S. Huettner, J. Bisquert, *Nat Commun* **2018**, *9*, 5113.
- [35] H. Jin, E. Debroye, M. Keshavarz, I. G. Scheblykin, M. B. J. Roeffaers, J. Hofkens, J. A. Steele, *Mater. Horiz.* **2020**, *7*, 397.
- [36] H. Kim, L. Zhao, J. S. Price, A. J. Grede, K. Roh, A. N. Brigeman, M. Lopez, B. P. Rand, N. C. Giebink, *Nat Commun* **2018**, *9*, 4893.
- [37] Y.-C. Zhao, W.-K. Zhou, X. Zhou, K.-H. Liu, D.-P. Yu, Q. Zhao, *Light Sci Appl* **2017**, *6*, e16243.
- [38] Y. Deng, Z. Xiao, J. Huang, *Adv. Energy Mater.* **2015**, *5*, 1500721.
- [39] V. Gulbinas, *physics* **2020**, *60*, DOI 10.3952/physics.v60i1.4160.
- [40] B. Chen, M. Yang, S. Priya, K. Zhu, *J. Phys. Chem. Lett.* **2016**, *7*, 905.
- [41] R. Jasiūnas, H. Zhang, J. Yuan, X. Zhou, D. Qian, Y. Zou, A. Devižis, J. Šulskus, F. Gao, V. Gulbinas, *J. Phys. Chem. C* **2020**, *124*, 21283.

## Acknowledgements

The authors acknowledge funding from the European Research Council (ERC) under the European Union's Horizon 2020 research and innovation programme (grant agreement № 835133, ULTRA-LUX) and funding from European Regional Development Fund (project No 01.2.2-LMT-K-718-03-0048) under grant agreement with the Research Council of Lithuania (LMTLT). W.Q. would like to thank the financial support of the postdoctoral fellowship grant from FWO.

# Supporting information

## Ion motion determines multiphase performance dynamics of perovskite LEDs

*Jevgenij Chmeliov, Karim Elkhoully<sup>#</sup>, Rokas Gegevičius, Lukas Jonušis, Andrius Devižis, Andrius Gelžinis, Marius Franckevičius, Iakov Goldberg, Johan Hofkens, Paul Heremans, Weiming Qiu, \* Vidmantas Gulbinas\**

### 1. Experimental

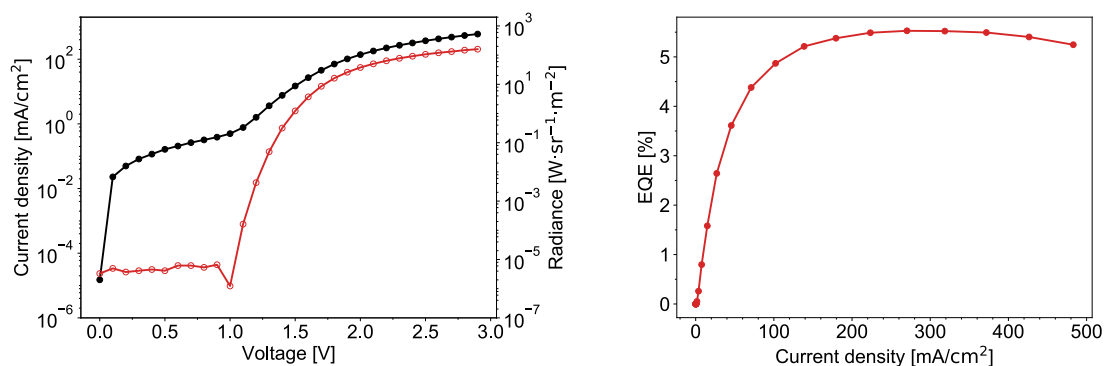


**Figure S1.** (a) J-V-R and (b) EQE-J characteristics for a stressed PeLED.

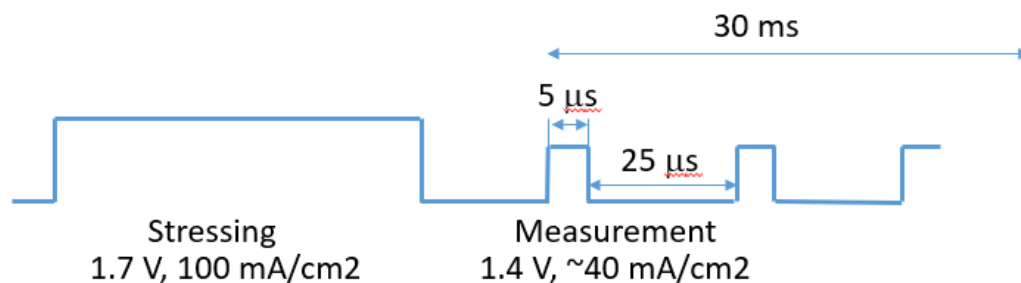


**Figure S2.** Protocol of pulsed measurements.

The sample was stressed for variable time duration and subsequently EL intensity, current and mean EL wavelength, were measured by applying train of short electrical pulses.

Photoluminescence, electroabsorption and capacitance were investigated by using the same stressing protocol, but measurements were performed at zero applied voltage.

## 2. Experimental results.

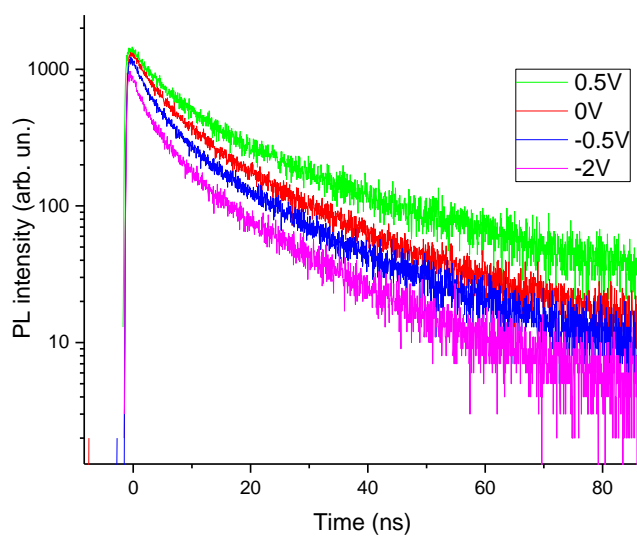


**Figure S3.** PL kinetics of the pristine PeLED at different applied voltages.

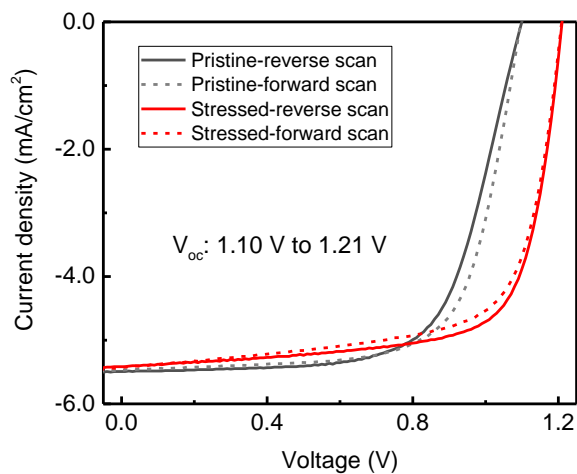


**Figure S4. Current-voltage dependence of the PeLED operating as solar cell under artificial solar illumination.**

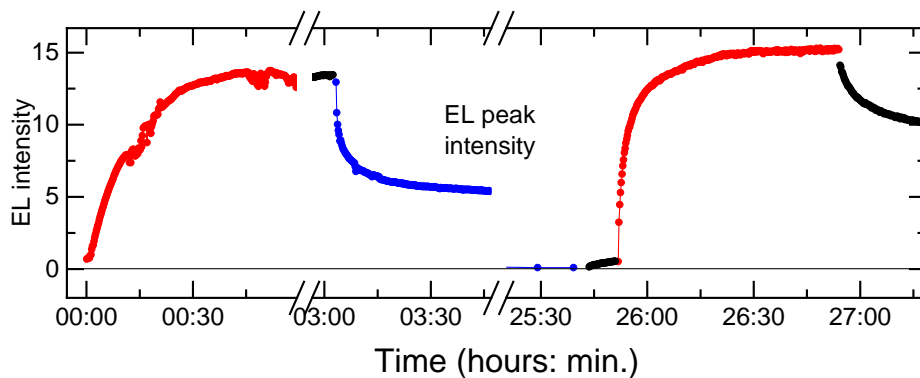


**Figure S5. EL intensity changes induced by positive and negative stressing voltages. Red points correspond to stressing by positive voltage, blue points - to application of negative voltage and black points - to relaxation at zero voltage.**

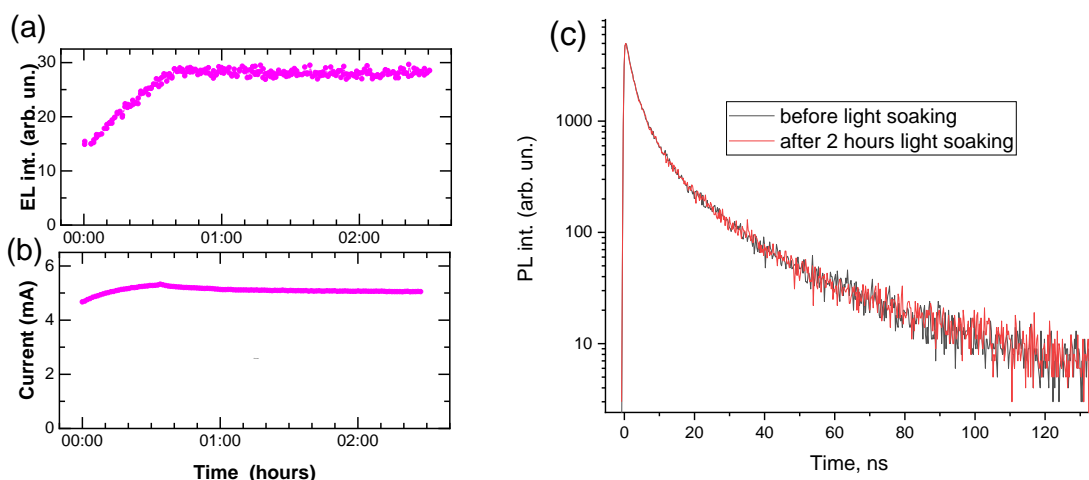


**Figure S6. Light soaking of pristine sample.** EL (a) and current (b) kinetics induced by sample soaking by 1 Sun light. EL intensity units were identical as in Figure 2, thus EL intensity created by light soaking was about 10 times lower than obtained by current stressing. (c) PL kinetics before and after light soaking.

### 3. Numerical calculations

The model used to numerically calculate ion and charge carrier dynamics is based on a number of parameters. These parameters are introduced in the Section 3 of the Main text as well as the model description below, while their numerical values are listed in Table S1.

#### Intrinsic electric field

As a result of the applied external voltage, some ions that are weakly bound to their lattice position start to diffuse through the perovskite material. If the total density of such “mobile” ions (and that of accumulated charge carriers, when the external voltage is supplied) is not extremely low, their produced electric field might introduce significant changes to the net electric field in the perovskite, which, in turn, will affect the ion and charge carrier dynamics therein.

We assume that the thickness of the perovskite layer,  $L$ , is much smaller than its lateral dimensions (i. e.  $L \ll \sqrt{S}$ , here  $S$  is the cross-section of the perovskite layer) and neglect any variations in the density of ions and charge carrier across the perovskite layer. Therefore, the electric field has only a single component along the  $x$  axis ( $0 \leq x \leq L$ ). If we denote the spatial density of free electrons and holes as  $n(x)$  and  $p(x)$ , the density of positive and negative ions

(or their vacancies)—as  $N_p(x)$  and  $N_n(x)$ , respectively, and assume that both types of ions are univalent, the resulting ion charge density distribution we be

$$\rho(x) = e \left( N_p(x) - N_n(x) + p(x) - n(x) \right), \quad (\text{S1})$$

here  $e$  is the elementary charge. By applying the Gauss law, one can easily find that the electric field at some point  $x$ , produced by this charge distribution  $\rho(x)$ , is

$$E_{\text{charge}}(x) = \frac{1}{2\varepsilon\varepsilon_0} \left[ \int_0^x \rho(x') dx' - \int_x^L \rho(x') dx' \right], \quad (\text{S2})$$

here  $\varepsilon\varepsilon_0$  is the electric permittivity of the perovskite medium. By integrating this expression over the coordinate, one can obtain the distribution of the electrostatic potential (with respect to the point  $x = 0$ ) within the perovskite due to inhomogeneous charge distribution:

$$\begin{aligned} \varphi_{\text{charge}}(x) &= - \int_0^x E_{\text{charge}}(x') dx' \\ &= \frac{1}{2\varepsilon\varepsilon_0} \int_0^x dx' \left[ - \int_0^{x'} \rho(x'') dx'' + \int_{x'}^L \rho(x'') dx'' \right]. \end{aligned} \quad (\text{S3})$$

By changing order of integration, the later expression can be simplified into

$$\varphi_{\text{charge}}(x) = \frac{1}{2\varepsilon\varepsilon_0} \left[ -x \int_0^x \rho(x') dx' + x \int_x^L \rho(x') dx' + 2 \int_0^x x' \rho(x') dx' \right]. \quad (\text{S4})$$

If there is some constant external voltage  $V_{\text{ext}}$  applied to the perovskite layer in addition to the (negative) built-in voltage  $V_{\text{bi}}$  (so that  $\varphi_{\text{ext}}(L) = V_{\text{ext}} + V_{\text{bi}} = V$ ), it produces homogeneous electric field

$$E_{\text{ext}} = \frac{\varphi_{\text{charge}}(L) - V}{L}, \quad (\text{S5})$$

so that the net electric field and electrostatic potential within the perovskite are

$$E(x) = E_{\text{ext}} + E_{\text{charge}}(x) \quad (\text{S6})$$

And

$$\varphi(x) = \frac{V - \varphi_{\text{charge}}(L)}{L} \cdot x + \varphi_{\text{charge}}(x). \quad (\text{S7})$$

### Charge carrier dynamics

Dynamics of the electrons and holes in the perovskite layer on the time scale of microseconds is described by the system of coupled Einstein–Smoluchovsky reaction–diffusion equations:

$$\begin{aligned} \frac{\partial n}{\partial t} &= \frac{\partial}{\partial x} \left[ -v_n n + D_n \frac{\partial n}{\partial x} \right] - \gamma n p, \\ \frac{\partial p}{\partial t} &= \frac{\partial}{\partial x} \left[ -v_p p + D_p \frac{\partial p}{\partial x} \right] - \gamma n p, \end{aligned} \quad (\text{S8})$$

here  $v_n(x, t) = -\mu_n E(x, t)$  and  $v_p(x, t) = \mu_p E(x, t)$  are the drift velocities of electrons and holes, respectively;  $D_n = \mu_n k_B T / e$  and  $D_p = \mu_p k_B T / e$  are their diffusion coefficients;  $\mu_n$  and  $\mu_p$  are their mobilities;  $\gamma$  is electron–hole recombination rate;  $k_B$  denotes the Boltzmann constant;  $T$  stands for the absolute temperature; and  $E(x, t)$  is the strength of the electric field at the time moment  $t$  at the spatial

point  $x$ , calculated according to Eq. S6 from the instantaneous densities of ions, their vacancies, and charge carriers. One should also note that due to the intrinsic electric field produced by the ions and charge carriers themselves, not only the net field  $E(x)$  becomes inhomogeneous, but also the diffusion equations S8 are spatially non-local.

The interface with the PCBM electron transport layer at  $x = 0$  is assumed to be the ideal source of electrons with the constant contact density  $n_{\text{cont}}$ ; at the interface with the PolyTPD layer ( $x = L$ ), we assume some leakage of the electrons with the rate constant  $k_n^{(\text{leak})}$ . The latter interface is also assumed to be the source of holes with the constant contact density  $p_{\text{cont}}$ ; however, the injection of holes into the perovskite is inhibited by the activation barrier  $\Delta E_{\text{act}}$  originating from the difference of the valence band energy in PolyTPD and the perovskite (see Fig. 1). Therefore, the density of holes  $p(L)$  in the perovskite is assumed to be somewhat smaller, in accordance to the thermodynamic equilibrium with  $p_{\text{cont}}$ . In our calculations, we additionally assumed that holes can partially tunnel through this barrier for the distance of  $\delta x$ , meaning that rapid gradient of electrostatic potential  $\varphi(x)$  at  $x = L$  results in higher contact hole density  $p(L)$  (this effect can be noted in Figs 7. d and f: we can see in panel (f) slightly larger gradient of electron energy at  $x = 40$  nm and  $t = 20$  s compared to the initial time  $t = 0$ ; accordingly, the hole density shown in panel (d) at  $x = 40$  nm and  $t = 20$  s is larger than at the initial time  $t = 0$ ). Finally, some leakage of the holes with the rate constant  $k_p^{(\text{leak})}$  at the interface with PCBM ( $x = 0$ ) is also assumed. All these effects can be expressed as the following boundary conditions of the Eqs. S8:

$$\begin{aligned} n(x=0) &= n_{\text{cont}}, \\ f_n(x=L) &= k_n^{(\text{leak})} \cdot n(L); \\ f_p(x=0) &= -k_p^{(\text{leak})} \cdot p(0), \\ p(x=L) &= p_{\text{cont}} \exp\left(-\frac{\Delta E_{\text{act}} - [V - \varphi(L - \delta x)]}{k_B T}\right), \end{aligned} \quad (\text{S9})$$

here  $f_n(x)$  and  $f_p(x)$  are the fluxes of electrons and holes, respectively:

$$f_n(x) = v_n n - D_n \frac{\partial n}{\partial x}, \quad f_p(x) = v_p p - D_p \frac{\partial p}{\partial x}. \quad (\text{S10})$$

Equations S8 were solved numerically using finite difference method (we used fixed spatial discretization of  $\Delta x = L/160$  while integration time steps were chosen adaptively) on the time scale of  $\mu\text{s}$  until the steady-state regime is reached. Since ions move on a much slower timescale of seconds, they were assumed to be “frozen” while calculating charge carrier dynamics. The resulting steady-state electron and hole densities, corresponding to the three distributions of ion densities shown in Fig. 7c (“snapshots” at  $t = 0, 20$  s, and 60s), are presented in Fig. 7d, while the corresponding spatial variations in the electron energy,  $-e\varphi(x)$ , are shown in Fig. 7f. The electric current density corresponding to these steady-state electron and holes distributions,

$$j = e[f_p(x) - f_n(x)], \quad (\text{S11})$$

does not depend on  $x$ , as follows from the charge conservation law.

## Ion diffusion

As already mentioned, ion diffusion occurs on much longer time scale (compared to the charge carrier dynamics) of tens of seconds. In our calculations, we assumed that the density of mobile negative iodine ions (if they were uniformly distributed across the perovskite) is  $N_{\text{ions}}$ ; their charge is partially

compensated by the immobile positive iodine ions vacancies, distributed uniformly with the density  $N_{\text{vac}}$  (i.e.  $N_{\text{p}} \equiv N_{\text{vac}} = \text{const}$ ). Iodine ion diffusion in the electric field  $E(x)$  is described by the Einstein–Smoluchovsky equation

$$\frac{\partial N_n}{\partial t} = \frac{\partial}{\partial x} \left[ -v_{\text{ion}} N_n + D_{\text{ion}} \frac{\partial N_n}{\partial x} \right], \quad (\text{S12})$$

here  $v_{\text{ion}}(x, t) = -\mu_{\text{ion}} E(x, t)$  and  $D_{\text{ion}} = \mu_{\text{ion}} k_{\text{B}} T / e$  are the drift velocity and the diffusion coefficient of the iodine ions, respectively;  $\mu_{\text{ion}}$  stands for the ion mobility; and  $E(x, t)$  is the strength of the electric field, calculated according to Eq. S6 from the instantaneous densities of ions, their vacancies, and charge carriers. Eq. S12 is supplemented with the natural zero-flux boundary conditions at the interfaces  $x = 0$  and  $x = L$ :

$$f_{\text{ion}}(0) = f_{\text{ion}}(L) = 0, \quad (\text{S13})$$

where ion flux is defined as

$$f_{\text{ion}}(x) = v_{\text{ion}} N_n - D_{\text{ion}} \frac{\partial N_n}{\partial x}. \quad (\text{S14})$$

Due to these boundary conditions the total number of iodine ions does not change in time:  $\int_0^L N_n(x, t) dx = N_{\text{ions}} L$ .

To calculate current and electroluminescence dynamics on the time scale of tens of seconds, we started from the initial ion distribution

$$N_n(x, t = 0) = N_{\text{ions}} \frac{|V_{\text{bi}}| e \exp\left(\frac{|V_{\text{bi}}| e}{k_{\text{B}} T} \cdot \frac{L-x}{L}\right)}{\exp\left(\frac{|V_{\text{bi}}| e}{k_{\text{B}} T}\right) - 1}, \quad (\text{S15})$$

corresponding to the steady-state solution of Eq. S12, when ions move in the homogeneous electric field produced by the built-in voltage  $V_{\text{bi}}$  (intrinsic electric field produced by ions themselves and vacancies is assumed to be screened-out by some free charge carriers). Such distribution might be not entirely correct, but that is fixed soon after application of the external voltage, when diffusion of ions and charge carriers is implicitly considered. We then applied external positive voltage  $V_{\text{ext}}$  and calculate the charge carrier dynamics according to Eqs. S8. The obtained results are the quantities shown in Fig. 7 that are denoted as corresponding to the time moment  $t = 0$ . In particular, we calculated the net electric field  $E(x, t = 0)$  that is created by the external voltage, built-in voltage, this initial distribution of ions and vacancies as well as the steady-state distribution. We then propagated Eq. S12 in time for the short time interval of  $\Delta t = 1$  s. Since during this short period neither ion density nor charge carrier densities changed significantly, for simplicity we also assumed that during this whole time period the electric field remained the same as it was at  $t = 0$ . Next, we again calculated charge carrier dynamics, now corresponding to the ion distribution at time  $t = \Delta t$ , and obtained the new total electric field  $E(x, t = \Delta t)$ . We then propagated Eq. S12 in time for another period of  $\Delta t$ . The whole procedure was repeated until the ion distribution reached its steady-state regime (corresponding to the homogeneous zero-flux,  $f_{\text{ion}}(x) = 0$ , for any  $x$ ), thus obtaining the kinetics presented in Fig. 7a.

**Table S1.** Model parameters used to calculate kinetics and distributions shown in Fig. 7 of the main text.

| Model parameter  | Notation         | Numerical value   |
|--|------------------|---|
| Built-in voltage   | $V_{bi}$         | -1 V  |
| Applied external direct voltage  | $V_{ext}$        | 0.6 V   |
| Relative permittivity of the perovskite layer                                  | $\epsilon$       | 20  |
| Iodine ions density  | $N_{ions}$       | $5.7 \cdot 10^{17} \text{ cm}^{-3}$                         |
| Iodine ion vacancies density   | $N_{vac}$        | 10% of $N_{ions}$   |
| Ion mobility   | $\mu_{ion}$      | $10^{-12} \text{ cm}^2/(\text{V}\cdot\text{s})$             |
| Electron mobility at 300, 240, and 200 K                                       | $\mu_n$          | 0.1, 0.017, and 0.005 $\text{cm}^2/(\text{V}\cdot\text{s})$ |
| Hole mobility  | $\mu_p$          | 0.1 $\text{cm}^2/(\text{V}\cdot\text{s})$                   |
| Electron–hole recombination rate   | $\gamma$         | 1500 $\mu\text{m}^3/\text{s}$                               |
| Electron leakage through the contact rate                                      | $k_n^{(leak)}$   | 0.001 cm/s  |
| Hole leakage through the contact rate  | $k_p^{(leak)}$   | 0.01 cm/s   |
| Electron contact density in the PCBM layer                                     | $n_{cont}$       | $26 \cdot 10^{12} \text{ cm}^{-3}$                          |
| Hole contact density in the PolyTPD layer                                      | $p_{cont}$       | $1100 \cdot 10^{12} \text{ cm}^{-3}$                        |
| Activation barrier for hole injection from the PolyTPD layer                   | $\Delta E_{act}$ | 0.2 eV  |
| Maximal tunneling distance for the injected holes                              | $\delta x$       | 1 nm  |
| Current stressing rate ( $j_{max}$ is the maximal (saturated) current density) | $k_{str}$        | $0.01 \text{ s}^{-1} / j_{max}$                             |

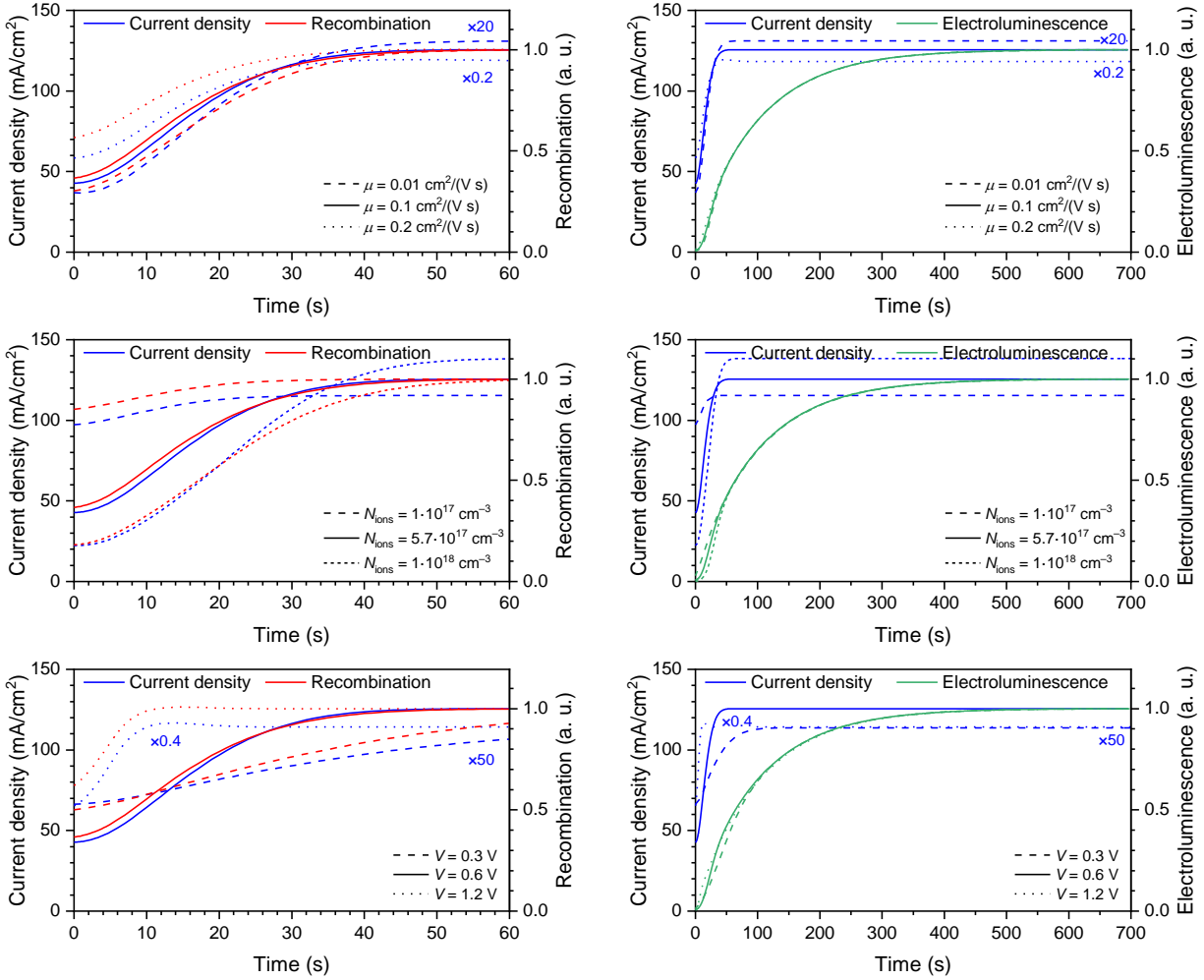


**Figure S6** Sensitivity of the calculated current and EL kinetics to the variations in model parameters: charge carrier mobility  $\mu_n = \mu_p = \mu$  (top), density of the mobile ions  $N_{\text{ions}}$  (middle) and applied external voltage  $V_{\text{ext}}$  (bottom). Left panels correspond to the current and electron–hole recombination kinetics (as in Fig. 7a of the Main text) and right panels present current and EL kinetics (similarly to Fig. 7b). Solid lines represent the same kinetics as in Fig. 7a and b, dashed lines—the result of the reduced parameter, dotted lines—the effect of the increased parameter. For better comparison of the relative amplitudes of the calculated kinetics, some of them were rescaled (the scaling factor is shown in the figure panels).

